Summary of Research
(Final Report)

# Simulation of Flow Control Using Deformable Surfaces

NASA Research Grant NAG 1-2018
Research Period: 17 March 1998 – 16 March 2001

Principal Investigator:
Prof. C. Randall Truman
Mechanical Engineering Department
University of New Mexico
Albuquerque, NM 87131
truman@unm.edu
505/277-6296

Submitted to:

Technical Contact:
Mr. William L. Sellers
NASA Langley Research Center
Mail Stop 170
Hampton VA 23681
757/864-2224

LaRC Grants Officer:
Ms. Carol Reddic
NASA Langley Research Center
Mail Stop 126
Hampton VA 23681
757/864-6042

## Abstract

The goal of this investigation is to numerically simulate the effects of oscillatory actuators placed on the leading edge of an airfoil, and to quantify the effects of oscillatory blowing on an airfoil stall behavior. It has been demonstrated experimentally that periodic blowing can delay flow separation at high angle of attack. The computations are to be performed for a TAU 0015 airfoil at a high Reynolds number of $\sim 1\times 10^6$ with turbulent flow conditions. The two-equation Wilcox $k-\omega$ turbulence model has been shown to provide reliable descriptions of transition and turbulence at high Reynolds numbers. The results are to be compared to Seifert's experimental data.


## Introduction

Studies indicate that when periodic flow excitation is applied to airfoils, it can effectively delay flow separation. There have been several approaches introduced to reduce flow separation, namely, deformation of the leading edge of an airfoil, steady blowing and several different methods of oscillatory blowing applied to the airfoil. This research is focused on steady or oscillatory blowing on the leading edge of an airfoil. Studies have indicated that oscillatory/periodic blowing is significantly more efficient than steady suction or steady blowing at controlling separation.[1,2,3] Not only that, the implementation of a controlled periodic excitation is more feasible than steady blowing.

Experiments on a NACA 0015 airfoil with low Reynolds number have shown that the incompressible maximum lift coefficient, $C_{l,max}$, can be increased by more than 15%. In addition, the post-stall lift can be increased by as much as 50% and post-stall drag can be reduced by more than 50%.[4] The airfoil that is currently being investigated is the TAU 0015, which was tested in

a low-speed wind tunnel at Tel-Aviv University (TAU). Finally, experiments performed over a wide range of Reynolds and Mach numbers showed that periodic excitation can effectively delay turbulent boundary layer separation and reattach flows.[1,2,3] Further research in active control has shown that Reynolds numbers corresponding to a jetliner at takeoff condition were successfully applied.[2] The numerical model being used is the compressible Navier-Stokes OSC2D code implementing the two-equation Wilcox $k$-$\omega$ turbulence model. Predictions will be compared with the experimental results produced by Seifert[5] as well as with the computational results from Joslin et al.[6] and Donovan et al.[7].

## Airfoil Geometry

A common practice in experiments is to use a blunt or finite thickness trailing edge. However, for computational and grid generation purposes we implement a sharp trailing edge. The NACA 00xx airfoils with a finite thickness trailing edge are described by

$$\frac{\bar{y}}{c} = \left(\frac{t/c}{0.20}\right)\left[a_0\left(\frac{\bar{x}}{c}\right)^{1/2} + a_1\left(\frac{\bar{x}}{c}\right) + a_2\left(\frac{\bar{x}}{c}\right)^2 + a_3\left(\frac{\bar{x}}{c}\right)^3 + a_4\left(\frac{\bar{x}}{c}\right)\right]^4 \qquad (1)$$

where $t/c$ is the thickness-chord ratio (e.g., $t/c = 0.15$ for a NACA 0015 airfoil). The constant coefficients for the equation (1) are: $a_0 = 0.2969$, $a_1 = -0.1260$, $a_2 = -0.3516$, $a_3 = 0.2843$ and $a_4 = -0.1015$.[8] The coefficient of the $x^2$ component is changed to $a_2 = -0.3537$, to convert the NACA 00xx airfoil from a blunt trailing edge to a sharp trailing edge.

The coordinate data for the TAU 0015 airfoil provided by Seifert includes a notch at the leading edge, a notch at $x/c \approx 0.76$ on the upper surface, and a finite thickness trailing edge. The notch on the upper surface will be ignored in this study. By using a similar approach to that

described above, the TAU 0015 data provided by Seifert was converted to a sharp trailing edge by the transformations

$$y = y_{data} - 0.001575(\tilde{x}_1)^2 \tag{2}$$

where $\tilde{x}_1 = \left(\frac{x + 0.00328}{1.00328}\right)$ is a function of the specified length for the upper surface of the airfoil, and

$$y = y_{data} + 0.001570(\tilde{x}_2)^2 \tag{3}$$

where $\tilde{x}_2 = \left(\frac{x + 0.00656}{1.00656}\right)$ is a function of the specified length for the lower surface of the airfoil. The difference between equations *(2)* and *(3)* is due to the definition of points on the trailing edge at the upper and lower surfaces.

Now, by modifying the NACA 0015 equation we can closely match the values produced from the equations above with $y = \bar{y}/c_0$ and $x = \bar{x}/c_0$, and let $c_0 = 1.0$ for comparison purposes. First, the upper surface of the airfoil is described by

$$y_{t1} = 0.75\left(a_0 x^{1/2} + a_1 x + a_2 x^2 + a_3 x^3 + a_4 x^4\right), \quad \text{for } 0.3 \le x \le 1.0 \tag{4.a}$$

and

$$y_{t2} = 0.75\left(a_0 x_1^{1/2} + a_1 x_1 + a_2 x_1^2 + a_3 x_1^3 + a_4 x_1^4\right), \quad \text{for } -0.00328 \le x < 0.3 \tag{4.b}$$

where, $x_1 = \left(x + 0.00328\right)\left(\frac{0.3}{0.30328}\right)$. The lower surface is described by

$$y_{b1} = -0.75\left(a_0 x^{1/2} + a_1 x + a_2 x^2 + a_3 x^3 + a_4 x^4\right), \quad \text{for } 0.3 \le x \le 1.0 \tag{4.c}$$

and

$$y_{b2} = -0.75\left(a_0 x_2^{1/2} + a_1 x_2 + a_2 x_2^2 + a_3 x_2^3 + a_4 x_2^4\right), \quad \text{for } -0.00656 \le x < 0.3 \tag{4.d}$$

where, $x_2 = (x + 0.00656)\left(\frac{0.3}{0.30656}\right)$. The coefficients $a_i$ are determined by least square fits of equations *(4)* to the respective portions of the sharp trailing edge TAU 0015.

The relative differences in y between the TAU 0015 sharp trailing edge airfoil described by equations *(1)-(3)* and the curve-fitted TAU 0015 airfoil described by equations *(4)* are less than $\pm 0.5\%$ with the exception of a couple points located near the discontinuity located at the notch on the leading edge, where the absolute difference in *y* were less than *0.0001.*

Now, we normalize the current curve-fitted TAU 0015 airfoil for computational purposes. The x-transformations are needed to make the leading edge (of the lower surface) coincide with the origin. We do this normalization and transformation by

$$x^* = \frac{x + 0.00656}{1.00656} \tag{5.a}$$

for both the lower and upper surfaces, then

$$y^* = \begin{cases} \dfrac{y_t}{1.00656} \\ \dfrac{y_b}{1.00656} \end{cases} \tag{5.b}$$

again, for the lower and upper surfaces which was defined in equations *(4).* The purpose of using a curve-fitted equation is to define the surface boundary of the airfoil continuously with the exception of the notch at the leading edge.

**Equations of Motion**

For compressible turbulent fluid flows, the equations of motion and $k-\omega$ turbulence model equations written in terms of Favre mass-averaged quantities are

Mass conservation:

$$\frac{\partial \rho}{\partial t}+\frac{\partial}{\partial x_j}\left(\rho u_j\right)=0 \tag{6}$$

Momentum balance:

$$\frac{\partial}{\partial t}\left(\rho u_i\right)+\frac{\partial}{\partial x_j}\left(\rho u_j u_i\right)=-\frac{\partial p}{\partial x_i}+\frac{\partial \tilde{\tau}_{ij}}{\partial x_j} \tag{7}$$

Mean energy conservation:

$$\frac{\partial}{\partial t}\left(\rho E\right)+\frac{\partial}{\partial x_j}\left(\rho u_j H\right)=\frac{\partial}{\partial x_j}\left[u_i \tilde{\tau}_{ij}+\left(\mu+\sigma^* \mu_T\right)\frac{\partial k}{\partial x_j}-q_j\right] \tag{8}$$

Turbulent mixing energy:

$$\frac{\partial}{\partial t}\left(\rho k\right)+\frac{\partial}{\partial x_j}\left(\rho u_j k\right)=\tau_{ij}\frac{\partial u_i}{\partial x_j}-\beta^* \rho \omega k+\frac{\partial}{\partial x_j}\left[\left(\mu+\sigma^* \mu_T\right)\frac{\partial k}{\partial x_j}\right] \tag{9}$$

Specific dissipation rate:

$$\frac{\partial}{\partial t}\left(\rho \omega\right)+\frac{\partial}{\partial x_j}\left(\rho u_j \omega\right)=\left(\frac{\alpha \omega}{k}\right)\tau_{ij}\frac{\partial u_i}{\partial x_j}-\beta \rho \omega^2+\frac{\partial}{\partial x_j}\left[\left(\mu+\sigma \mu_T\right)\frac{\partial \omega}{\partial x_j}\right] \tag{10}$$

where $t$ is time, $x_i$ is the position vector, $u_i$ is the velocity vector, $\rho$ is density, p is pressure, $\mu$ is molecular viscosity, $\tilde{\tau}_{ij}$ is the sum of molecular and Reynolds stress tensors, and $q_j$ is the sum of the molecular and turbulent heat flux vectors. In Equation *(8)*, the quantities $E = e + k + u_i u_j / 2$ and $H = h + k + u_i u_i / 2$ are total energy and enthalpy, respectively, where $h = e + p / \rho$, and $e$ and $h$ denote internal energy and enthalpy, respectively. Additionally, $\tau_{ij}$ is the Reynolds stress tensor.

The turbulent mixing energy $k$ and the specific dissipation rate $\omega$ are needed to define the eddy viscosity[9]

$$\mu_T = \alpha^* \frac{\rho k}{\omega} \tag{11}$$

The total viscous stress tensor is

$$\tilde{\tau}_{ij} = 2\mu\left[S_{ij} - \left(\frac{1}{3}\right)\frac{\partial u_k}{\partial x_k}\delta_{ij}\right] + \tau_{ij} \tag{12}$$

where the mean strain-rate tensor $S_{ij}$ is

$$S_{ij} = \frac{1}{2}\left(\frac{\partial u_i}{\partial x_j} + \frac{\partial u_j}{\partial x_i}\right) \tag{13}$$

We invoke the Boussinesq approximation that the Reynolds stress tensor is proportional to the mean strain-rate tensor

$$\tau_{ij} = 2\mu_T\left[S_{ij} - \left(\frac{1}{3}\right)\frac{\partial u_k}{\partial x_k}\delta_{ij}\right] - \frac{2}{3}\rho k\delta_{ij} \tag{14}$$

Finally, the heat flux vector $q_j$ is approximated as

$$q_j = -\left(\frac{\mu}{Pr_L} + \frac{\mu_T}{Pr_T}\right)\frac{\partial h}{\partial x_j} \tag{15}$$

where $Pr_L$ and $Pr_T$ are the laminar and turbulent Prandtl numbers, respectively. The closure coefficients[9] are $\beta = 3/40$, $\beta^* = 9/100$, $\alpha = 5/9$, $\alpha^* = 1$, $\sigma = 1/2$ and $\sigma^* = 1/2$.

## Governing Equations

The method used to formulate the flow governing equations past an airfoil makes use of an inertial reference frame in which any movement of the airfoil is simulated by multiple grid generation as the airfoil moves. The way to get around the multiple grid generation if the wing movement is predefined and the body is rigid. In this case, a single grid is generated for the problem and new grids are obtained by solving a set of equations based on rigid body rotation as the airfoil goes through its pitching motion. However, if the body is flexible or deforming, this method will not work. Hence, the multiple grid generation used to track the wing motion is more general and can handle both flexible and deforming bodies. The latter approach, combined with a moving grid, has been adopted here.

Arbitrary shaped bodies present a difficulty for finite difference formulation of the problem in Cartesian coordinates. So, we need to map the physical space into a uniform computational space using a general curvilinear coordinate transformation. For the problem under study, the grid is moving in the physical space, so time must be included as one of the variables in the general coordinate transformation.

Since wish to simulate deep dynamic stall, the full Navier-Stokes equations in nondimensional and conservative-law form are written as

$$Q_t + E_x + F_y = \mathrm{Re}^{-1}\left(E_{vx} + F_{vy}\right) \tag{16}$$

where

$$Q = \begin{pmatrix} \rho \\ \rho u \\ \rho v \\ e \end{pmatrix},\ E = \begin{pmatrix} \rho u \\ \rho u^2 + p \\ \rho uv \\ u(e+p) \end{pmatrix},\ F = \begin{pmatrix} \rho v \\ \rho uv \\ \rho v^2 + p \\ v(e+p) \end{pmatrix}$$

$$E_v = \begin{pmatrix} 0 \\ \tau_{xx} \\ \tau_{yx} \\ E_{v4} \end{pmatrix}, \quad F_v = \begin{pmatrix} 0 \\ \tau_{xy} \\ \tau_{yy} \\ F_{v4} \end{pmatrix},$$

with

$$\tau_{xx} = (\lambda + 2\mu)u_x + \lambda v_y,$$

$$\tau_{xy} = \mu(u_y + v_x),$$

$$\tau_{yx} = \tau_{xy},$$

$$\tau_{yy} = (\lambda + 2\mu)v_y + \lambda u_x,$$

$$E_{v4} = u\tau_{xx} + v\tau_{xy} + \frac{\mu}{(\gamma - 1)\mathrm{Pr}}(a^2)_x,$$

$$F_{v4} = u\tau_{xy} + v\tau_{yy} + \frac{\mu}{(\gamma - 1)\mathrm{Pr}}(a^2)_y,$$

where *Re* is the Reynolds number, *Pr* is a Prandtl number and $\gamma$ is the ratio of specific heats (1.4 for air). The speed of sound $a$ is given for ideal fluids by $a^2 = \gamma p/\rho$. The dynamic viscosity $\mu$ is calculated from Sutherland's formula and Stokes hypothesis $\lambda + (2/3)\mu = 0$ is assumed. Pressure is related to the conservative flow variables, $Q$, by the equation of state

$$p = (\gamma - 1)\left[e - \frac{1}{2}\rho(u^2 + v^2)\right]. \tag{17}$$

Equation (16) is based on an Eulerian description of motion. In this approach, a fixed control volume is used and the changes to the fluid are recorded as the fluid passes through the control volume. The choice of nondimensional parameters is arbitrary. The variables $\rho$ (density), $u$ and $v$ (Cartesian velocities), $e$ (total energy), $t$ (time), and $\mu$, are scaled by

$$\tilde{\rho}=\frac{\rho}{\rho_\infty},\ \tilde{u}=\frac{u}{a_\infty},\ \tilde{v}=\frac{v}{a_\infty},\ \tilde{e}=\frac{e}{\rho_\infty a_\infty^2},\ \tilde{t}=\frac{ta_\infty}{l},\ \tilde{\mu}=\frac{\mu}{\mu_\infty},$$

$$\mathrm{Re}=\frac{\rho_\infty l a_\infty}{\mu_\infty},$$

where $\infty$ refers to free stream quantities and $l$ represents a reference length such as the chord of an airfoil. Note that the Reynolds number uses freestream speed of sound $a_\infty$ rather than the usual $u_\infty$, therefore it must be scaled by $M_\infty = u_\infty / a_\infty$. For the remainder of this development the $\sim$ will be dropped for simplicity.

## Curvilinear Coordinate Transformation

The Navier-Stokes equations can be transformed from Cartesian coordinates to general curvilinear coordinates where

$$\tau = t,$$

$$\xi = \xi(x,y,t), \tag{18}$$

$$\eta = \eta(x,y,t).$$

The coordinate transformation, or computational space, introduced here are chosen so that the grid spacing in the curvilinear space is uniform and of unit length. This produces a computational space $\xi$ and $\eta$ which is a rectangular domain of uniform unit cells. Therefore, the standard unweighted differencing schemes can be used in the numerical formulation. There will be a one to one correspondence between a point in computational space and a point in physical space except for regions where there are cuts due to topology or singularities. In those cases, it may be necessary to map one physical point to many computational points that normally occurs at computational boundaries.

The mapping relations are constructed through chain rule expansions, which are used to represent the Cartesian derivatives $\partial_x$ and $\partial_y$ of Eq. (16) in terms of the curvilinear derivatives where in matrix form

$$\begin{bmatrix} \partial_t \\ \partial_x \\ \partial_y \end{bmatrix} = \begin{bmatrix} 1 & \xi_t & \eta_t \\ 0 & \xi_x & \eta_x \\ 0 & \xi_y & \eta_y \end{bmatrix} \begin{bmatrix} \partial_\tau \\ \partial_\xi \\ \partial_\eta \end{bmatrix} \tag{19}$$

In most cases the transformation from physical space to computational space is not known analytically, rather it is generated numerically. This is accomplished by reversing the role of the independent variables in the chain rule formulas, Eq. (19), to get

$$\begin{aligned} \partial_\tau &= \partial_t + x_\tau \partial_x + y_\tau \partial_y, \\ \partial_\xi &= x_\xi \partial_x + y_\xi \partial_y, \\ \partial_\eta &= x_\eta \partial_x + y_\eta \partial_y \end{aligned} \tag{20}$$

and in matrix form

$$\begin{bmatrix} \partial_\tau \\ \partial_\xi \\ \partial_\eta \end{bmatrix} \begin{bmatrix} 1 & x_\tau & y_\tau \\ 0 & x_\xi & y_\xi \\ 0 & x_\eta & y_\eta \end{bmatrix} \begin{bmatrix} \partial_t \\ \partial_x \\ \partial_y \end{bmatrix} \tag{21}$$

Solving Eq. (21) to expand curvilinear derivatives $\partial_\tau$, $\partial_\xi$ and $\partial_\eta$ in the terms of Cartesian derivatives can be written in matrix form

$$\begin{bmatrix} \partial_t \\ \partial_x \\ \partial_y \end{bmatrix} = \begin{bmatrix} 1 & x_\tau & y_\tau \\ 0 & x_\xi & y_\xi \\ 0 & x_\eta & y_\eta \end{bmatrix}^{-1} \begin{bmatrix} \partial_\tau \\ \partial_\xi \\ \partial_\eta \end{bmatrix} \tag{22}$$

By evaluating equations (19) and (22) we get

$$\xi_t = -x_\tau \xi_x - y_\tau \xi_y$$

$$\eta_t = -x_\tau \eta_x - y_\tau \eta_y$$

$$\xi_x = J y_\eta \tag{23}$$

$$\eta_x = -J y_\xi$$

$$\xi_y = -J x_\eta$$

$$\eta_y = J x_\xi$$

where the metric Jacobian, $J$, is defined by

$$J^{-1} = x_\xi y_\eta - x_\eta y_\xi \tag{24}$$

and $x_\tau$, $y_\tau$ are grid velocity components. Equation (16) after coordinate transformation using chain rule becomes

$$\begin{aligned} &Q_\tau + \xi_t Q_\xi + \eta_t Q_\eta + \xi_x E_\xi + \eta_x F_\eta + \xi_y E_\xi + \eta_y F_\eta \\ &= \mathrm{Re}^{-1}\left[\xi_x (E_v)_\xi + \eta_x (E_v)_\eta + \xi_y (F_v)_\xi + \eta_y (F_v)_\eta\right] \end{aligned} \tag{25}$$

## Invariants of Transformation

At this point of the development of the governing equations one can stop and use Eq. (25) to solve the flow field. It should be noted that Eq. (25) is not in a full divergence form, since metrics appear as coefficients in the above differential equations. Therefore, the flow properties are not strongly conserved. There are researchers who advocate the use of so-called "chain rule form" in problems such as shock capturing. Here, we shall restrict ourselves to the strong conservation law form, which will be derived below. Let us produce the strong conservation law form using Eq. (25). First we multiply this equation by $J^{-1}$ and use the chain rule on all the terms, such as

$$J^{-1}\xi_x \partial_\xi E = \partial_\xi \left( \frac{\xi_x}{J} E \right) - E \partial_\xi \left( \frac{\xi_x}{J} \right) \tag{26}$$

and collect all the terms into two parts.

(Part 1)

$$\begin{aligned} &\left(J^{-1}Q\right)_\tau + \left[J^{-1}\left(\xi_t Q + \xi_x E + \xi_y F\right)\right] + \left[J^{-1}\left(\eta_t Q + \eta_x E + \eta_y F\right)\right] \\ &= \mathrm{Re}^{-1}\left\{\left[J^{-1}\left(\xi_x E_v + \xi_y F_v\right)\right]_\xi + \left[J^{-1}\left(\eta_x E_v + \eta_y F_v\right)\right]_\eta\right\} \end{aligned} \tag{27}$$

(Part 2)

$$\begin{aligned} &-Q\left[\left(\frac{1}{J}\right)_\tau + \left(\frac{\xi_t}{J}\right)_\xi + \left(\frac{\eta_t}{J}\right)_\eta\right] \\ &-E\left[\left(\frac{\xi_x}{J}\right)_\xi + \left(\frac{\eta_x}{J}\right)_\eta\right] - F\left[\left(\frac{\xi_y}{J}\right)_\xi + \left(\frac{\eta_y}{J}\right)_\eta\right] \\ &= \mathrm{Re}^{-1}\left\{-E_v\left[\left(\frac{\xi_x}{J}\right)_\xi + \left(\frac{\eta_x}{J}\right)_\eta\right] - F_v\left[\left(\frac{\xi_y}{J}\right)_\xi + \left(\frac{\eta_y}{J}\right)_\eta\right]\right\} \end{aligned} \tag{28}$$

If the latter part, Eq. (28), is eliminated then the strong conservation law form of the equations results in Part 1 equaling zero. For example, take the following term in Eq. (28)

$$\left(\frac{\xi_x}{J}\right)_\xi + \left(\frac{\eta_x}{J}\right)_\eta$$

and substitute for $\xi_x$ and $\eta_x$ to get

$$\left(y_{\eta\xi} - y_{\xi\eta}\right) + \left(y_{\xi\eta} - y_{\eta\xi}\right) \tag{29}$$

Now analytically differentiation is commutative and each of the above terms in then sums to zero, thus eliminating Part 2 or Eq. (28). Then equation Eq. (27) represents the strong conservation law form of Eq. (25). Further simplification of Eq. (27) using $U$ and $V$, contravariant velocities, results in

$$\left(\hat{Q}\right)_\tau + \left(\hat{E}\right)_\xi + \left(\hat{F}\right)_\eta = \mathrm{Re}^{-1}\left[\left(\hat{E}_v\right)_\xi + \left(\hat{F}_v\right)_\eta\right] \tag{30}$$

where

$$\hat{Q} = J^{-1}\begin{pmatrix}\rho\\ \rho u\\ \rho v\\ e\end{pmatrix},\quad \hat{E} = J^{-1}\begin{pmatrix}\rho U\\ \rho u U + \xi_x p\\ \rho v U + \xi_y p\\ (e+p)U - \xi_t p\end{pmatrix},$$

$$\hat{F} = J^{-1}\begin{pmatrix}\rho V\\ \rho u V + \eta_x p\\ \rho v V + \eta_y p\\ (e+p)V - \eta_t p\end{pmatrix},$$

$$\hat{E}_v = J^{-1}\begin{pmatrix}0\\ \xi_x\tau_{xx} + \xi_y\tau_{xy}\\ \xi_x\tau_{yx} + \xi_y\tau_{yy}\\ \xi_x E_{v4} + \xi_y F_{v4}\end{pmatrix},\quad \hat{F}_v = J^{-1}\begin{pmatrix}0\\ \eta_x\tau_{xx} + \eta_y\tau_{xy}\\ \eta_x\tau_{yx} + \eta_y\tau_{yy}\\ \eta_x E_{v4} + \eta_y F_{v4}\end{pmatrix},$$

with the contravariant velocities defined as

$$U = \xi_t + \xi_x u + \xi_y v,$$

$$V = \eta_t + \eta_x u + \eta_y v$$

and the stress terms are

$$\tau_{xx} = \frac{2}{3}\mu\left[2\left(\xi_x u_\xi + \eta_x u_\eta\right) - \left(\xi_y v_\xi + \eta_y v_\eta\right)\right],$$

$$\tau_{yy} = \frac{2}{3}\mu\left[-\left(\xi_x u_\xi + \eta_x u_\eta\right) + 2\left(\xi_y v_\xi + \eta_y v_\eta\right)\right],$$

$$\tau_{xy} = \mu\left[\xi_y u_\xi + \eta_y u_\eta + \xi_x v_\xi + \eta_x v_\eta\right]$$

Equation 30 represents the transformed governing flow equations in their final form. The implementation of the numerical method and its solution procedure are presented below.

## Boundary Conditions

Probably the most important aspect in successful application of any numerical technique is the proper treatment of boundary conditions, including impermeable boundaries such as solid wall and permeable boundaries such as inflow and outflow boundaries, which allow mass across their surfaces.

A slip boundary condition is assigned on each tunnel wall, since the boundary layers on these walls cannot be resolved due to the limited number of grid points. In computational space, it is relatively easy to compute the velocity on the surface by means of extrapolating the contravariant velocity components. This procedure not only extrapolates the velocity components but also extrapolates the associated local contravariant base vectors which results in severe mesh-dependency of the solution. To correct the problem, it is not necessary to extrapolate the contravariant velocity but rather the tangential velocity components (physical space). This is done by linear first-order extrapolation, which sets the normal gradient of the velocity and other flow parameters equal to zero. For example, on an $\eta$-constant plane the velocity component $u$ is computed by setting

$$\frac{\partial u}{\partial n} = \nabla u \cdot \hat{n} = 0 \tag{31}$$

where $\hat{n}$ is a unit normal vector defined as

$$n = \frac{\eta_x \hat{i} + \eta_y \hat{j}}{\sqrt{\eta_x^2 + \eta_y^2}}. \tag{32}$$

Combining Eq. (32) into Eq. (31) we get

$$\left(\xi_x \eta_x + \xi_y \eta_y\right) u_\xi + \left(\eta_x^2 + \eta_y^2\right) u_\eta = 0 \tag{33}$$

Equation (33) is solved for $u$ implicitly in the $\xi$-direction. Similarly, other variables can be extrapolated. On the surface of the wing, the no-slip boundary condition is specified. From Eq. (30) it is apparent that we have four dependent variables at every grid point. In order to update these variables at the surface, four equations are required. To obtain the correct velocity of the surface (wing), the contravariant velocities

$$\begin{aligned} U &= \xi_x (u - x_\tau) + \xi_y (v - y_\tau) \\ V &= \eta_x (u - x_\tau) + \eta_y (v - y_\tau) \end{aligned} \tag{34}$$

are set to zero at the body ($\eta$-constant plane). To extract the Cartesian velocity components $u$ and $v$ from Eq. (34), it is necessary to do a backward transformation from computational space to physical space, using

$$\begin{bmatrix} u \\ v \end{bmatrix} = J^{-1} \begin{bmatrix} \eta_y & -\xi_y \\ -\eta_x & \xi_x \end{bmatrix} \begin{bmatrix} U - \xi_t \\ V - \eta_t \end{bmatrix}. \tag{35}$$

A relation for pressure along the body surface is obtained by combining the two transformed momentum equations

$$\begin{aligned} & P_n \left(\eta_x^2 + \eta_y^2\right)^{1/2} = \left(\xi_x \eta_x + \xi_y \eta_y\right) p_\xi + \left(\eta_x^2 + \eta_y^2\right) p_\eta \\ & = \rho \left[ \partial_\tau \eta_t + u \partial_\tau \eta_x + v \partial_\tau \eta_y \right] \end{aligned} \tag{36}$$

The above relation for pressure boundary condition was found to produce virtually the same results as the simpler $\partial p / \partial n = 0$ condition in this study. However, relation (36) is more stable. Equations (34) and (36) provide a total of three equations. The fourth equation is obtained through specifying either constant wall temperature or an adiabatic wall. For the latter case which is used here,

$$\frac{\partial T}{\partial n} = 0$$

must be satisfied at the wall. Assuming a perfect gas law, we have the following relation between pressure, density and temperature

$$p = \rho RT .$$

Differentiating the above relation with respect to $n$ and using the adiabatic condition and the assumption that $\partial p/\partial n$ is zero between the wall and the first line of discretization adjacent to it, we have

$$\frac{\partial \rho}{\partial n} = 0 .$$

This equation can be written in computational space as

$$\left(\xi_x \eta_x + \xi_y \eta_y\right) p_\xi + \left(\eta_x^2 + \eta_y^2\right) p_\eta = 0 \qquad (37)$$

To obtain pressure and density, Equations (36) and (37) are implicitly solved in the $\xi$-direction. In the case of constant surface temperature, density at the wall is computed using the equation of state as

$$\rho_s = \frac{p_s}{RT_{wall}}$$

where subscript $s$ denotes properties at the surface. Now, with the addition of Eq. (37), there are five equations. Therefore, all conservative variables can be computed at the wall.
For the inflow boundary, conservative variables are set to free-stream conditions. First-order extrapolation is used to update variables on the outflow boundary.

There is a fictitious boundary condition or branch cut introduced by the coordinate transformation. The branch cut, which in this case is a plane, as shown in Figure 1, starts from trailing edge of the wing and extends up to the downstream boundary. Every point on this plane is represented by two points in the computational space. To correctly treat this boundary, it is

necessary to apply a periodic condition at the branch cut. This would result in a periodic block tridiagonal matrix which needs to be inverted at each time step. Periodic block tridiagonal inversion is much more costly than standard block tridiagonal inversion. Also, accuracy would require grid smoothness across the branch cut, which is difficult to obtain. However, due to the nature of the grid there is sufficient point clustering near the plane making it possible to extrapolate properties from interior nodes to two corresponding points in the computational space. Since every two points represents one point in a physical space, values there must be the same. Thus, an averaged value between the two corresponding points is computed and assigned to both points.

The boundary conditions described in this section have not been incorporated into the implicit formulation, but are lagged behind one time step. The resulting code is flexible and can be adapted to different problems with a moderate amount of work. However, it is difficult to judge what happens to the practical accuracy of the method at the boundary due to this type of implementation. Visbal & Shang[10] have evaluated implicit Navier-Stokes solvers in two-dimensions. They showed that for unsteady flow past a cylinder both implicit and explicit implementations of boundary conditions over the range of $\Delta\tau$ (0.005-0.01) produced virtually identical results.

For inviscid calculations, the slip condition is imposed on the surface of the wing. This is done in the computational space with the use of contravariant velocity components. Pressure is implicitly evaluated on the body using the unsteady form of the inviscid momentum equation.

$$\left(\eta_x^2+\eta_y^2\right)^{1/2}\rho_\eta =$$
$$\rho\left[\left(\eta_t\right)_\tau + u\left(\eta_x\right)_\tau + v\left(\eta_y\right)_\tau\right] - \rho U\left(\eta_x u_\xi + \eta_y v_\xi\right) - \rho V\left(\eta_x u_\eta + \eta_y u_\eta\right) =$$
$$\left(\xi_x\eta_x + \xi_y\eta_y\right)P_\xi + \left(\eta_x^2+\eta_y^2\right)P_\eta$$

Furthermore, the pressure on the no-slip portion of the slot at the leading edge is

$$\left(\xi_x^2+\xi_y^2\right)^{1/2}\rho_\eta =$$
$$\rho\left[\left(\xi_t\right)_\tau + u\left(\xi_x\right)_\tau + v\left(\xi_y\right)_\tau\right] - \rho U\left(\xi_x u_\xi + \xi_y v_\xi\right) - \rho V\left(\xi_x u_\eta + \xi_y u_\eta\right) =$$
$$\left(\xi_x^2+\xi_y^2\right)P_\xi + \left(\xi_x\eta_x + \xi_y\eta_y\right)P_\eta$$

Free stream stagnation enthaply is held constant along the body. Using the equation of enthalpy. For the far-field, the non-reflecting characteristic boundary condition is used. This boundary condition requires a mapping between the normal and tangential component of velocities and the Cartesian component of velocities. Dr. Steinberg used the Symbolic Manipulation code Macsyma to construct this mapping[11].

For viscous calculations, the no-slip condition is applied on the surface of the wing by setting the contravariant velocity components to zero. Pressure is evaluated in a same manner as in the inviscid case, using the inviscid momentum equation. For the wall temperature, either an adiabatic condition or constant wall temperature are used. Density is computed using a zero gradient condition normal to the surface for an evaluated using zeroth-order extrapolation and for the far-field a non-reflecting characteristic boundary condition is used. The wake is evaluated by using an overlapping scheme for both the inviscid and viscous cases.

## Grid Topology

A two dimensional C-grid will be used in this investigation of the TAU 0015 airfoil due to the high Reynolds number. The C-grid by its nature is not suitable for periodic boundary conditions in the $\xi$-direction and to apply a true periodicity condition across the branch cut in the C-grid, the $\eta$-sweep of the approximate factorization algorithm must be modified. The numerical finite difference code OSC2D implements the block pentadiagonal inversion and the cost is approximately less than two times the standard approach. The solution to the periodicity

problem developed by Visbal and Shang[12] is to overlap the branch cut region in the computational domain. This approach was verified in solving a 2-D Poisson equation in fully curvilinear coordinates using both O and C type grids. The results have shown that the concept is sound and can be applied to airfoil computations using the C-grid. Based, on the experimentation, it was determined that a five point overlap in the wake is sufficient to produce a smooth solution across the cut.[11] For the TAU 0015 airfoil, the grid topology is shown in Figure 1. The overlapping process in Figure 1 is shown by letting point B be the same point as B', point A is A' and so on. The polygon region of B-C-D-E-F-G-B is the iblank region of the grid. The term iblank indicates that a specified area of the grid is voided and no calculations are performed in that region.

## Approach and Discussion

The experiments conducted by Seifert[5] used actuators at several locations operated at various frequencies with Mach number 0.15 and Reynolds number 1.2 million. However, this report is focused on the TAU 0015 with the actuator located at the leading edge with different frequencies and blowing coefficients.

The different actuator boundary conditions that are being considered are introduced by the following oscillatory forcing functions

$$f(\xi) = \begin{cases} 1 \\ \sin(\pi\xi) \\ \sin^2(\pi\xi) \end{cases}, \tag{15}$$

where $\xi$ is the tangential direction to the surface. The jet suction/blowing is introduced through the velocity at the surface,

$$\vec{v}_{jet}(\xi,\eta=0,t)=\sqrt{\frac{c}{2H}}U_{\infty}\left[\sqrt{c_{\mu}}+\sqrt{2\langle c_{\mu}\rangle}\sin\left(F^{+}\frac{2\pi U_{\infty}t}{c}\right)\right]f(\xi)\vec{e}_{jet}, \tag{16}$$

where $\eta$ denotes the direction normal to the surface and $\vec{e}_{jet}$ determines the angle the jet makes with the surface. The spatial variation of the jet is specified by $f(\xi)$ and determines an effective jet width,

$$H=\int[f(\xi)]^2 d\xi, \tag{17}$$

where the integral is evaluated across the jet $(0\le\xi\le a)$. The non-dimensional frequency is $F^{+}=fc/U_{\infty}$, which relates the period of the jet cycle to the convection time of the flow over the airfoil. The steady momentum blowing coefficient, $c_{\mu}=2(H/c)(U_{jet}/U_{\infty})^2$, and the oscillatory momentum blowing coefficient, $\langle c_{\mu}\rangle\equiv 2(H/c)(\langle u'_{jet}\rangle/U_{\infty})^2$, determine the amplitude of the jet, where $U_{jet}$ is the mean jet velocity and $\langle u'_{jet}\rangle$ is the RMS velocity of the jet oscillations. The flow profile that behaves better and produces a nearly identical flow[7] is $sin^2(\pi\xi)$. The rest of the boundary on the airfoil surface is prescribed as a no-slip boundary.

In a previous study, predictions with an unstructured coarse grid showed some disagreement with measurements in the highly separated region in stall.[6] Furthermore, computations performed by Donovan et al.[6] and Joslin et al.[7] had trouble in predicting $\Delta C_l$ versus $\Delta\langle c_{\mu}\rangle$ where the experimental relation is monotonically increasing while the the numerical predictions are not. The approach herein is to use a fine, structured C-grid with the OSC2D finite difference code. The discontinuity of the blowing notch at the leading edge has caused some problems that will be overcome using the commercial package Gridgen to generate the geometric topology of the airfoil. The grid generated by Gridgen near the notch in the

leading edge is shown in Figure 3. The OSC2D code applies the two-equation Wilcox $k$-$\omega$ turbulence model, with the assumption of a turbulent boundary layer starting from the leading edge. Furthermore, the two-equation $k-\omega$ model has been shown to provide reasonably accurate description of turbulent and transitional flows in adverse pressure gradients.[9,13] Computational results including the lift and pressure coefficients versus the normalized chord position and the angle of attack will be compared with Seifert's experiment, as well as with the predictions of Donovan et al.[6] and Joslin et al.[7]

For all computations in this study, the equations of motion have been integrated through the viscous sublayer. The Wilcox $k-\omega$ model requires no special viscous damping functions to make possible integration through the sublayer. Viscous corrections by Wilcox[9] are needed only to improve transition predictions and to simulate subtle features of sublayer structure. The mean-flow properties are set according to no-slip and adiabatic-wall conditions. The no-slip condition also dictates that $k$ vanishes at solid boundaries. Furthermore, we have implemented the slightly-rough surface boundary condition for $\omega$. Finally, the blowing portion of the slot is treated differently, where $k$ and $\omega$ are evaluated using zeroth-order extrapolation.

Results are presented for oscillatory blowing at 4° angle of attack. Other angles of attack are being computed and will be published along with a comparison of the increase in lift coefficient provided by the oscillatory blowing.

Figures 2a-e show the oscillatory blowing on the leading edge at the different times in one cycle beginning with zero blowing velocity, progressing to maximum blowing at one-quarter cycle, back to zero blowing velocity at one-half cycle, then to maximum blowing at three-quarter cycle, and finally back to zero blowing velocity to complete the cycle. This cycle begins after one full cycle has been completed and the results have reached periodic conditions. Fig. 2a

shows separation off the leading edge of the slot with a large recirculating zone. Fig. 2b shows strong vortex development due to shear between the flow over the leading edge and the blowing from the slot. A larger view shows these vortices being convected downstream where they have significant influence on separation on the upper surface of the airfoil at higher angles of attack. Fig. 2d shows strong interaction between the flow over the leading edge and the region above the slot where fluid is being removed by suction.

## References


1. Seifert, A., Koss, T., Shepshelovich, M. and Wygnanski, I., "Oscillatory Blowing, a Tool to Delay Boundary Layer Separation", AIAA Journal, Vol. 31, Nov. 1993, pp.2052-2060.
2. Seifert, A. and Pack, L. G., "Oscillatory Control of Separation at High Reynolds Numbers", AIAA Journal, Vol. 37, No. 9, Sept. 1999, pp.1062-1071.
3. Pack, L. G. and Seifert, A., "Periodic Excitation for Jet Vectoring and Enhanced Spreading", AIAA-99-0672, Jan. 1999, 37th AIAA Aerospace Sciences Meeting and Exhibit, Reno, NV.
4. Seifert, A. and Pack, L. G., "Oscillatory Excitation of Unsteady Compressible Flows over Airfoils at Flight Reynolds Numbers", AIAA 99-0925, Jan. 1999, 37th AIAA Aerospace Sciences Meeting and Exhibit, Reno, NV.
5. Seifert, A., 1999, personal communication.
6. Joslin, R. D., Horta, L. G. and Chen, F., "Transitioning Active Flow Control to Applications", AIAA-99-3735, June-July 1999, 30th AIAA Fluid Dynamics Conference, Norfolk, VA.
7. Donovan, J. F., Kral, L. D. and Cary, A. W., "Active Flow Control Applied to an Airfoil", AIAA-98-0210, Jan. 1998, 36th Aerospace Sciences Meeting and Exhibit, Reno, NV.
8. Ladson, C. L., Brooks, C. W., Hill, A. S. and Sproles, D. S., "Computer Program To Obtain Ordinates for NACA Airfoils", NASA Technical Memorandum 4741, Dec. 1996.
9. Wilcox, D. C., "Simulation of Transition with a Two-Equation Turbulence Model", AIAA Journal, Vol. 32, No. 2, Feb. 1994, pp.247-255.
10. Visbal, M. R. and Shang, J. S., "Comparative Study Between 2 Navier-Stokes Algorithms for Transonic Airfoils," AIAA Journal, Vol. 24, pp. 599-606, 1986.

11. Roache, P. J., Salari, K., Truman, C. R., and Wilcox, D. C., "Dynamic Stall Control Study and Source Code", SBIR No. A90-158, Phase II Final Report, Nov. 1994.

12. Visbal, M. R. and Shang, J. S., "Investigation of the Flow Structure around a Rapidly Pitching Airfoil", AIAA Journal, Vol. 27, pp. 1044-1051, 1989.

13. Salari, K. and Roache, P. J., "Numerical Simulation of Dynamic Stall Using the Two-Equation K-w Turbulence Model", Advances in Computational Methods in Fluid Dynamics, ASME FED Vol. 196, June 1994, pp.1-7.

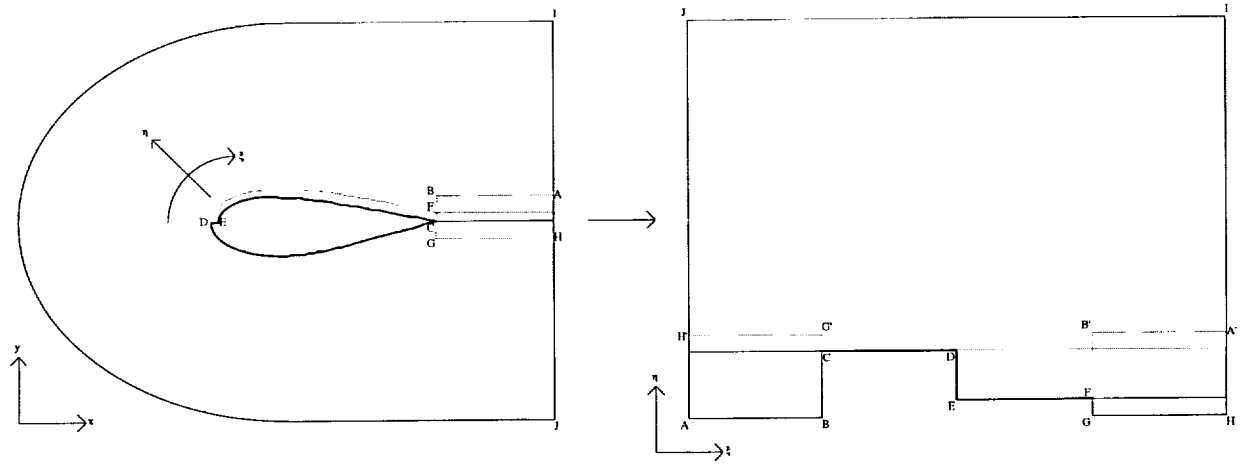

Figure 1. The coordinate transform between physical domain and computational domain for TAU 0015 airfoil.

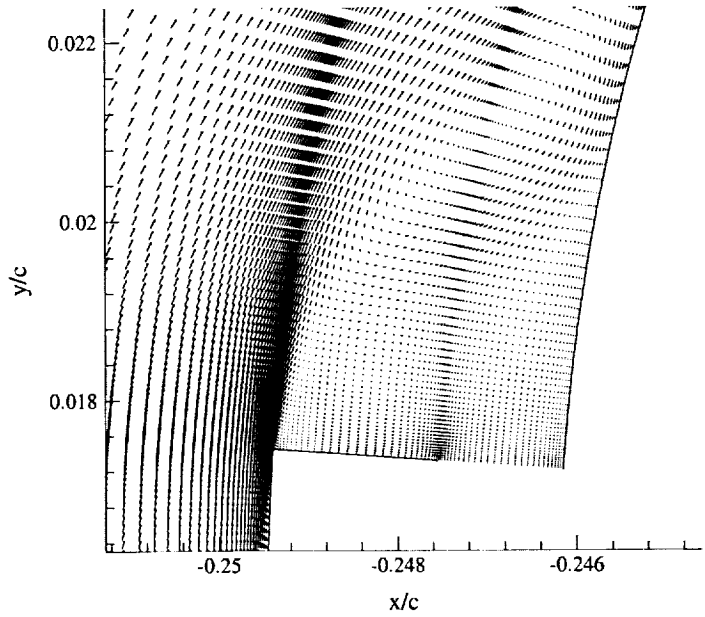


Figure 2a. Velocity vectors at the leading edge of the TAU 0015 airfoil at the beginning of an oscillatory blowing cycle (zero velocity at slot).

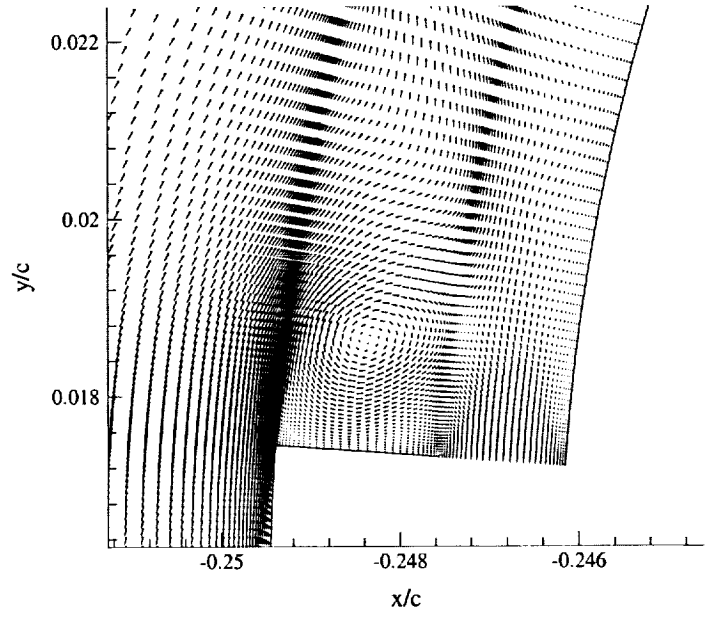


Figure 2b. Velocity vectors after one-quarter cycle of oscillatory blowing (maximum blowing at slot).

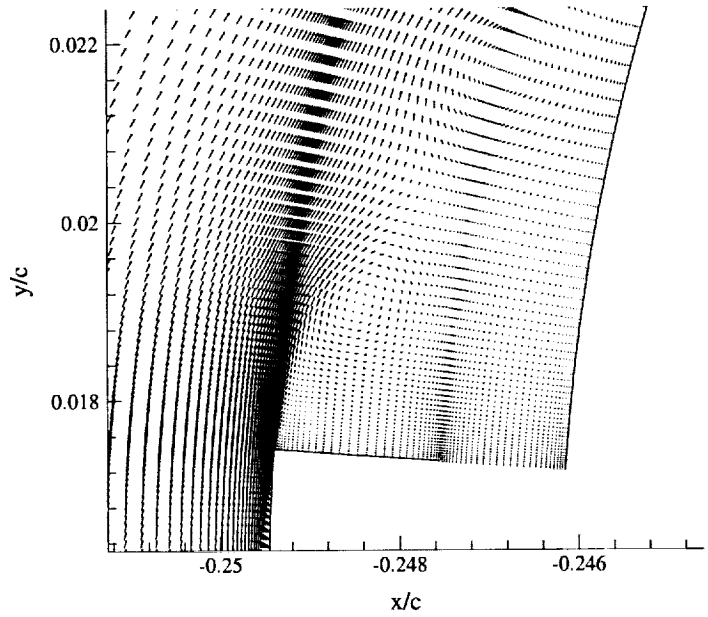


Figure 2c. Velocity vectors after half cycle of oscillatory blowing (zero velocity at slot).

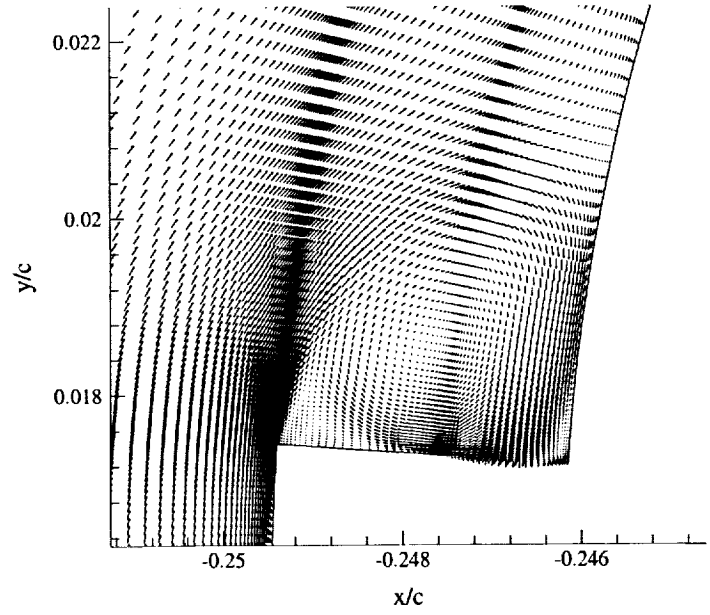


Figure 2d. Velocity vectors after three-quarter cycle of oscillatory blowing (maximum suction).

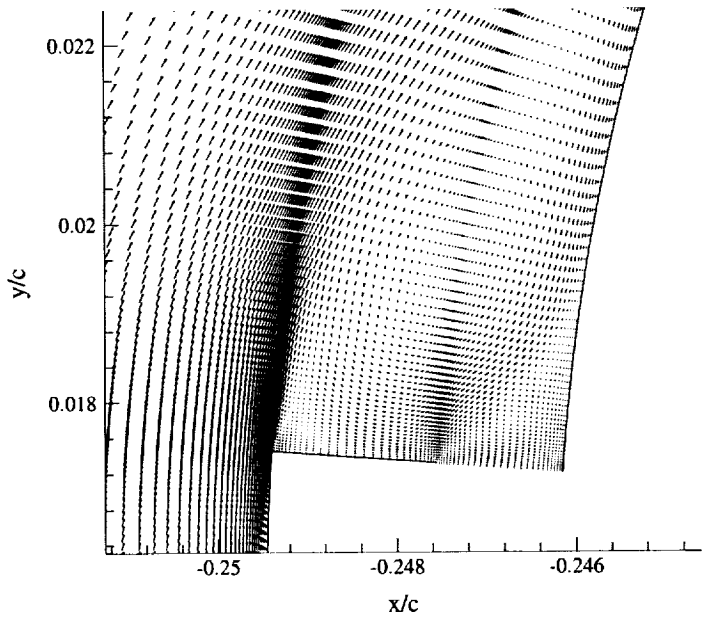


Figure 2e. Velocity vectors after a full cycle of blowing (zero velocity at slot)

.

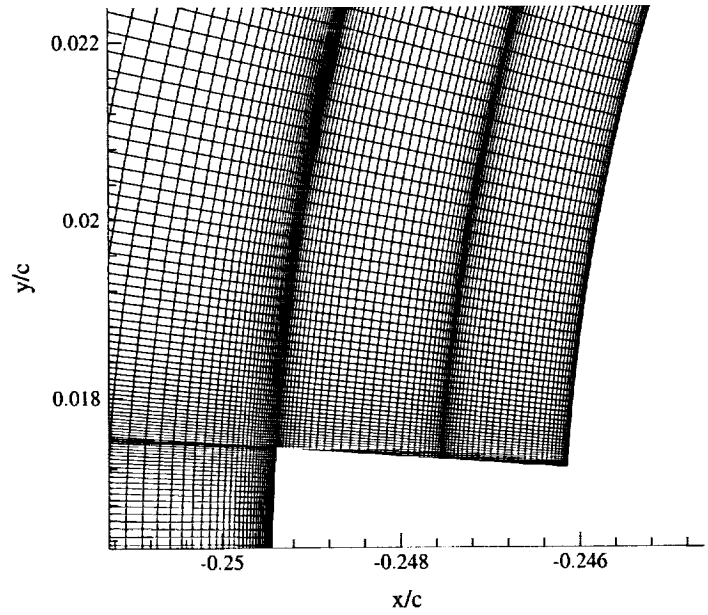


Figure 3. The grid structure at the leading edge of the airfoil.